Miniature piezoelectric actuators: design concept, fabrication and performance evaluation

1998 Smart Mater. Struct. 7 312

(http://iopscience.iop.org/0964-1726/7/3/007)

Smart Mater. Struct. **7** (1998) 312–326. Printed in the UK PII: S0964-1726(98)91229-0

Miniature piezoelectric actuators: design concept, fabrication and performance evaluation

C K Lee†, S H Chang‡ and Pei-Zen Chang†

† Institute of Applied Mechanics, National Taiwan University, Taipei, Taiwan, Republic of China
‡ Department of Mechanical Engineering, National Taiwan University, Taipei, Taiwan, Republic of China

Received 2 August 1997, accepted for publication 17 October 1997

Abstract. Magnifying mechanisms, which include bimorph configurations, waveguides, resonance, mechanical levers etc, that can convert a large-force, small-displacement piezoelectric material to become a smaller-force, large-displacement actuator are examined in detail. Sputtering processes for zinc oxide and lead–zirconate–titanate films, which are important for fabricating miniature laminated piezoelectric actuators, are presented. A newly developed laser Doppler interferometer that is especially designed for evaluating the performance of miniature piezoelectric actuators is also described. The design concept, optimization process, fabrication techniques and evaluation approach for such things as a piezoelectric impact hammer, a resonant dual-dimensional piezoelectric scanner, a Langevin type ultrasonic motor and a high-precision piezoelectric positioning stage are also discussed.

1. Introduction

Many of the recent advancements of micro-machining technologies have been in the area of sensing devices (MacDonald 1990, Baltes 1993, Ohara *et al* 1993, Motamedi and White 1994, Marty *et al* 1995, Storgarrd-Larsen *et al* 1995). However, the drive to search for high-powered actuators that are capable of packing a high energy density into a small volume has been increasing in importance as we move towards more practical micro-systems (Tai *et al* 1988, *Mechanical Engineering* 1992). Out of all the potential approaches, piezoelectric actuators stand to be one of the most promising technologies. No matter whether it is the new design concept, processing techniques or metrology methodologies, new approaches are needed to meet the ever more demanding research, development and manufacturing needs of producing miniature piezoelectric actuators. In this article, the underlying principle and viewpoint that lead to the development of many new tools and many new devices within the micro-electro-mechanical system research collectives of the National Taiwan University (NTU MEMS Collective) will be discussed in detail.

An examination of the literature shows that the flat and curved laminated bimorph types of actuator (Mason 1950, Rogacheva 1980, Bailey and Hubbard 1985, Lee and Moon 1989a, b, Lee 1990, Tzou and Gadre 1989, Tzou and Zhong 1994, Rogacheva 1994, Sonti and Jones 1996a, b) are the most common configurations used to transform the large-force, small-displacement characteristics of piezoelectric actuators. The ZnO (zinc oxide) and PZT (lead, zirconate and titanate) sputtering processes that seem promising for making the above-mentioned laminated bimorph types of miniature piezoelectric actuator will be examined as well.

Compared to laminated bimorph types of miniature piezoelectric actuator, devices based on piezoelectric stack

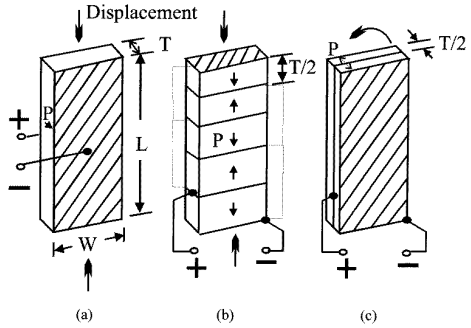

Comparison of different piezoelectric actuating types

	Displacement	Force Generated	Electro-mechanical Energy Transfer Efficiency	Resonant Frequency
(a) Single Layer	Low	Medium	Medium	Medium
(b) Stack	Medium	High	High	High
(c) Bimorph	High	Low	Low	Low

Figure 1. Some common piezoelectric actuating types.

0964-1726/98/030312+15$19.50

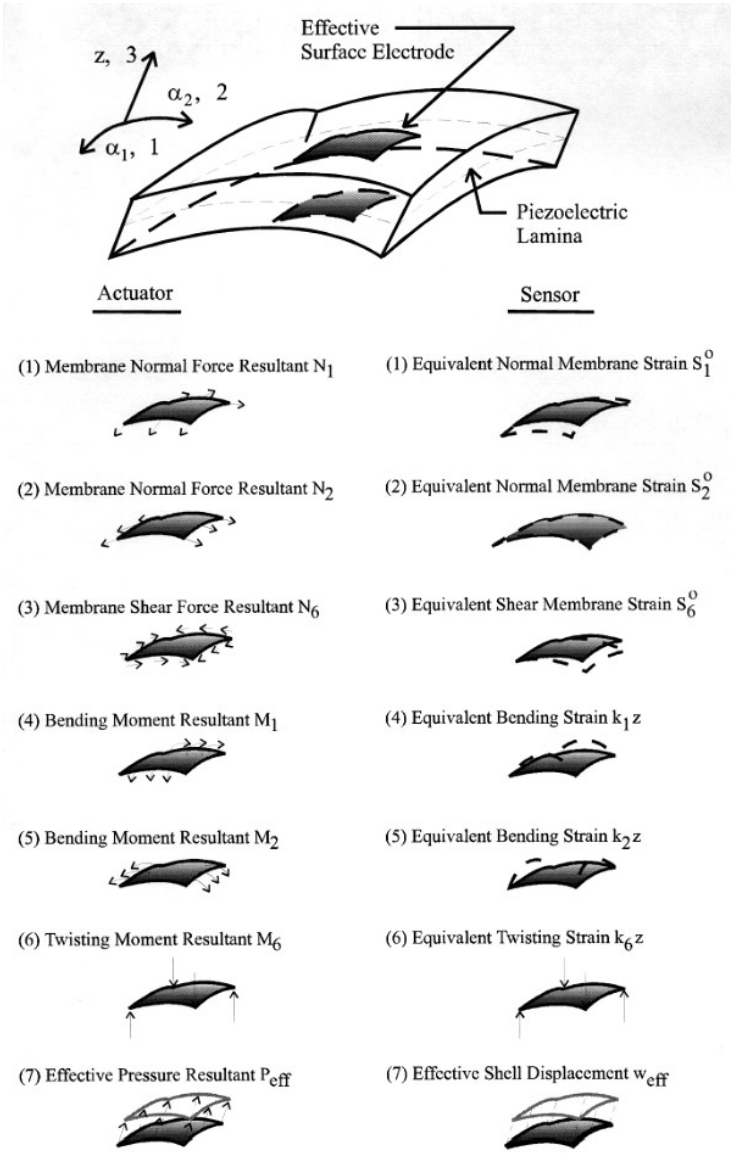

Figure 2. Reciprocal relationship between laminated shell based actuators and sensors.

actuators are gaining ever more emphasis due to their capabilities to output significantly more force. Piezoelectric stack actuators stacking piezoelectric layers into a stack to reduce the voltage level needed to obtain the same amount of displacement/force use the d_{33} mode (Chang and Wang 1988, 1990, Lee and Wu 1993, Wu and Lee 1994a, b). As piezoelectric stack actuators do not have the geometric effect on their side similar to that of the bimorph type of actuator, methodologies that transform the large-force, small-displacement characteristics of piezoelectric actuators need to be developed further to facilitate the use of these types of actuator. A comparison of these types of actuator is listed in figure 1. We can see that both the single-layer and the bimorph type belong to the laminated actuator type. It is clear from figure 1 that piezoelectric actuators of the laminated bimorph type can generate more displacement than piezoelectric stack actuators. However, piezoelectric stack actuators are generally capable of outputting much more force than laminated piezoelectric actuators.

In top-level thinking, adopting piezoelectric material in a laminated bimorph type of configuration is just like using a mechanical transformer to transform the generic large-force, small-displacement piezoelectric material characteristics into a small-force, large-displacement configuration. Other mechanical-transformer configurations include using the lever principle, the waveguide configuration and driving piezoelectric actuators in resonant modes. Design examples based on this design concept will be examined in detail. Four devices powered by using piezoelectric stack actuators and designed by using a waveguide, the lever principle and resonant effects (Chang and Wang 1988, 1990, Lee and Wu 1993, Wu and Lee 1994a, b) will be presented to illustrate this line of thinking within the NTU MEMS Collective. A newly developed laser Doppler interferometry system specifically designed for piezoelectric micro-actuators is also examined.

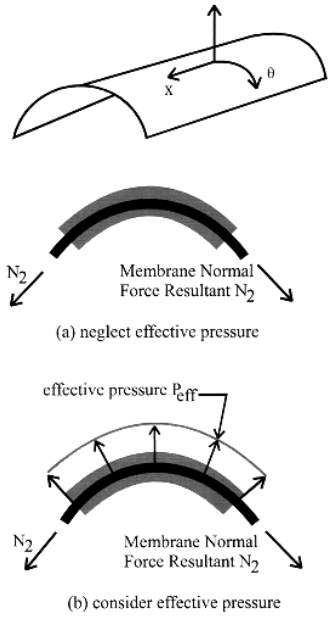

Figure 3. Effect of neglecting effective pressure in shell type structures.

2. Laminated bimorph type actuators

The laminated bimorph type of piezoelectric actuator drives the d_{31}, d_{32} and d_{36} mode of piezoelectric materials. Some of the early research work in this area is related to laminated piezoelectric beams, plates and shells (Bailey and Hubbard 1985, Lee 1987, Lee and Moon 1989a, b, Lee 1990, Tzou and Gadre 1989, Tzou and Anderson 1992, Tzou 1992, Tzou and Zhong 1994, Rogacheva 1994, Sonti and Jones 1996a, b).

The fundamental concept in designing laminated piezoelectric actuators is to use the reciprocal relationship as shown in figure 2. In addition, the superposition principle is used to understand the action of laminated piezoelectric actuators (Lee and Moon 1989a, b, Lee 1990, Tzou and Gadre 1989, Tzou and Zhong 1994, Rogacheva 1994, Sonti and Jones 1996a, b, Chou 1997). Out of all the seven resultants shown in figure 2, the effective pressure resultant P_{eff} appears only in curved actuators. In the past, when designing curved actuators, P_{eff} is a resultant that has been traditionally neglected. Experimental as well as theoretical results show that P_{eff} should be a very important factor when designing curved piezoelectric actuators. Considering the free flying shell shown in figure 3 and using only the first six resultants of figure 2 to examine the free-body diagram (figure 3(a)), we see results which show that a curved piezoelectric lamina can exert forces on the mass center of the shell. This error violates the fundamental principle of laminated piezoelectric actuators and must be corrected by imposing the P_{eff} (figure 3(b)).

For making miniature piezoelectric actuators, the sputtering process is one of the most promising techniques currently available. Two of the most common piezoelectric materials which are currently employed are ZnO and PZT, both of which can be deposited by using the sputtering process. The processing conditions and equipment developed will be described herein.

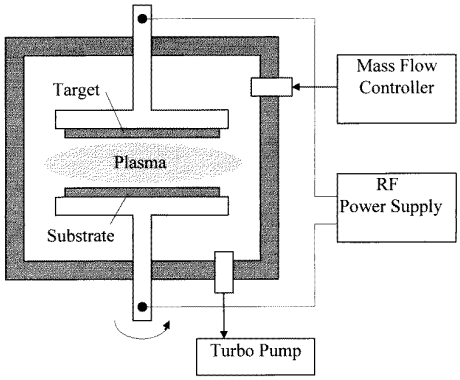

Figure 4. Schematic of a sputtering system.

To deposit ZnO film on silicon substrates, a RF magnetron sputtering is used in the process developed for constructing ZnO based actuators. The sputtering system (figure 4) used in our process is composed of three major parts. The first part consists of a vacuum chamber equipped with a turbo pump for gas evacuation, a mass flow controller for inlet gas regulation and a water pump for chamber-wall cooling. The second part includes a rotatable substrate holder for seating the silicon wafer and a target holder located above the substrate holder to hold the ZnO target wafer. The third part embodies a 13.6 MHz, 200 watts RF power supply for plasma generation. Adjustable settings in this self-designed and local-built system include chamber pressure, gas flow rate, substrate temperature and RF power levels.

Before ZnO is deposited, a layer of silicon dioxide (SiO_2) is first grown on the silicon substrate using either dry or wet oxidation. Depending on the final performance requirement, a patterned aluminum film can be deposited by an e-gun evaporation. With the substrate processed and cleaned, it can be placed onto the substrate holder. The ZnO target is then fixed in the target holder and adjusted to about 4 cm from the substrate. After the chamber has been evacuated to a pressure below 10^{-5} Torr, argon gas is introduced in the chamber to a pressure of 0.1 Torr. The influx of the argon gas is then adjusted to a flow rate of 100 sccm. Once the RF power is fed into the chamber to ignite the plasma, ZnO atoms knocked out by the plasma begin to deposit on the substrate.

Experimental data obtained from the chamber indicate that the deposition rate is mainly affected by the substrate temperature and RF power level. For example, at a 200 °C substrate temperature, the deposition rate on SiO_2 was 0.3 μm h^{-1} at a power level of 100 watts. At 0.6 μm h^{-1}, the power level was 150 watts, and at 1.4 μm h^{-1}, it was 200 watts. It is clear from our data that the deposition rate increases with the power level. However, x-ray diffraction data also suggest that the crystal orientation of ZnO films grown at the above-mentioned high-powered, high-temperature conditions is not well aligned. With a processing condition development, the process adopted now is the same conditions mentioned above except for

heating the substrate to 100 °C. In this chosen condition, the ZnO deposition rate will be reduced to 0.37 μm h^{-1} at 150 watts, which is nearly 50% lower than that at the 200 °C processing condition. In comparison, the deposition rate of aluminum is 0.35 μm h^{-1} under the same condition. The ZnO and aluminum films processed under the chosen conditions were inspected by using x-ray diffraction. The power diffraction pattern obtained from the x-ray diffraction revealed a single peak at 34.68° with a FWHM (full width at half maximum) of 0.3° which suggests a well aligned ZnO *c*-axis. More specifically, ZnO films with *c*-axis perpendicular to the substrate are sputtered on both the SiO_2 and aluminum coated silicon substrates at a rate of about 0.35 μm h^{-1} successfully in our newly constructed RF magnetron sputtering system. Integrating this process with other miniature structure construction steps can lead to more efficient miniature piezoelectric actuator designs and fabrication procedures.

To deposit PZT in this RF magnetron sputtering machine, the basic condition and operating procedures are identical to that of the ZnO. Instead of using ZnO as the target, PZT sputtering used a poled PZT block as the target. Traditionally, a thin layer of SiO_2, platinum or titanium is deposited at the top of the silicon substrate before the PZT is sputtered. To extend the applicability of PZT based actuators, PZT was sputtered on silicon, copper, platinum, gold and electroformed nickel substrate. Both x-ray diffraction and the Sawyer/Tower measurement (Radiant Technologies 1992) were used to identify the best PZT processing conditions in the magnetron sputtering machine. Compared to the ZnO sputtering rate, the PZT sputtering rate at 25 °C, 0.01 Torr, 100 sccm was found to be 0.067 μm h^{-1} for 50 watts, 0.583 μm h^{-1} for 100 watts and 1.083 μm h^{-1} for 150 watts. This deposition rate is comparable to ZnO if not faster. The scanning electron microscope (SEM) photos shown in figure 5 indicate that a PZT sputtered at a higher power will have a larger grain size.

Experimental results obtained indicate that once PZT film is sputtered, annealing processes including heating the sample from 700 to 900 °C and then gradually reducing the temperature within 5 to 60 minutes are needed to induce the alignment of the PZT domains. The x-ray diffraction (XRD) diagrams shown in figure 6 clearly indicate that the annealing process is generally needed to have the deposited PZT film exert piezoelectric effect. It was found that sputtering a PZT target onto electroformed nickel substrate at 150 watts power, and then annealing at 700 °C for 20 minutes arrived at the PZT film with the strongest polarization profile so far.

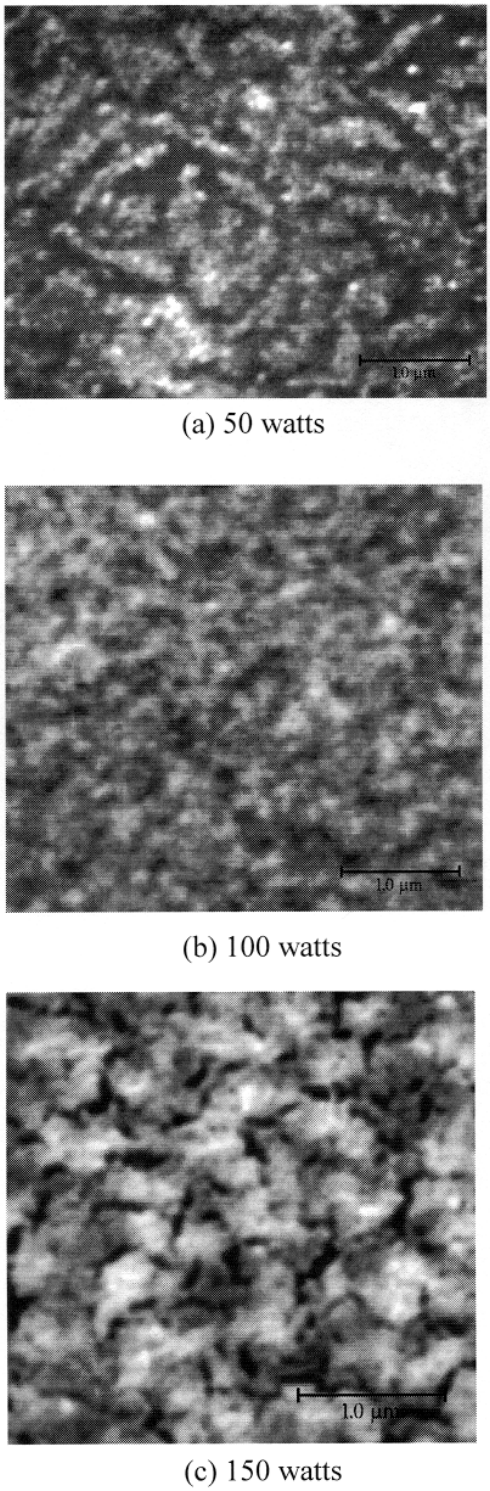

Figure 5. SEM photos of PZT thin film on silicon substrate processed under different sputtering power conditions.

3. Advanced laser Doppler interferometer

To satisfy the demands of micro-electromechanical systems and high-performance piezoelectric actuators, the performance evaluation tools must be improved rapidly. Metrology instrumentation that possesses both a wide bandwidth and high resolution is urgently needed in the field of precision engineering. Laser Doppler interferometers/vibrometers (Lee and Wu 1992, 1995, Lee *et al* 1996) have long been widely accepted as practical and effective tools for velocity and displacement analysis. In today's versatile and complicated measurement situations, most traditional interferometers are finding it difficult to keep up with the current high-tech development pace. Compared with traditional optical metrology instruments,

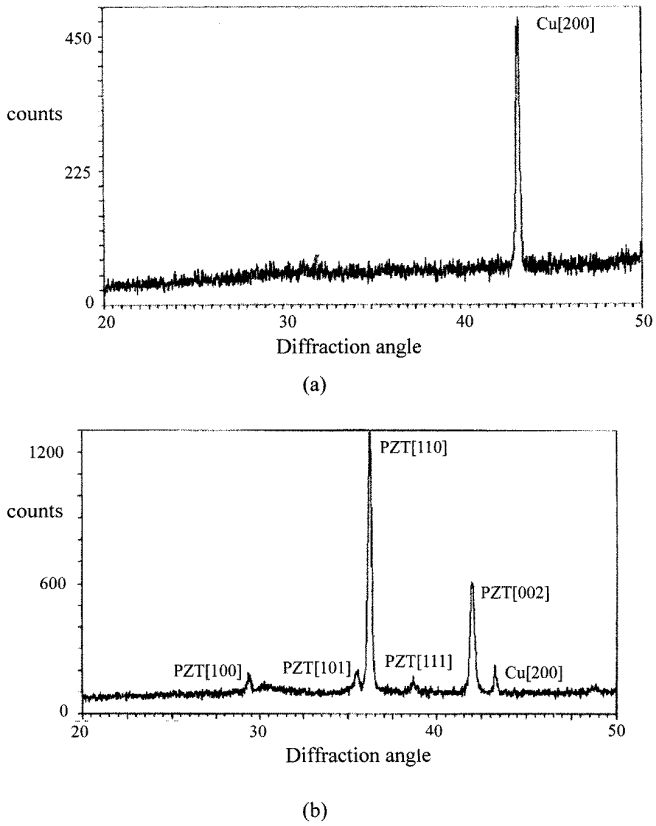

Figure 6. The x-ray diffraction diagram of PZT thin films sputtered on copper substrate before (a) and after (b) annealing at 750 °C for 20 minutes.

interferometers with features such as (1) no modification to measurement surfaces necessary, (2) is capable of absolute/differential detection, (3) is able to accommodate samples with significantly different reflectivity, (4) has nanometer resolutions and (5) possesses a megahertz bandwidth seem well suited to be adopted to examine ultra-high-precision high-performance miniature piezoelectric actuating systems.

The advanced vibrometer/interferometer device (AVID) described herein follows the fundamental principles of laser interferometry (Lee *et al* 1996, AHEAD 1997). Two basic optical layouts of this system, which can be easily converted back and forth by simply pulling a sliding stage, are shown in figure 7(a) and 7(b). Light beams from a He–Ne laser or collimated visible diode laser are split into two interference arms by a polarization beamsplitter PBS1. These light beams 1 and 2 are both linearly polarized and are orthogonal with respect to each other. The light beam 1 passes through a right-angle mirror and a polarization beamsplitter PBS2; it is focused to a point on the test target by a doublet lens L1. Light beam 2 passes through a similar path. The outgoing light beams and returning object beams are diametrically incident on different locations of focusing lenses L1 and L2. The two returning object beams remain linearly polarized and orthogonal with respect to each other after being recombined at PBS1. One thing that should be noted is that changes in the polarization states of the two returning light beams may occur in some measurement surfaces. To fully utilize the incident light energy, and maintaining maximum freedom in placing the two light beams and the orthogonally linear polarized states, a second polarization beamsplitter PBS2 is added to the optical path. More specifically, a circular polarization interferometry configuration is utilized to remove the directional ambiguity. One right circularly polarized light beam and one left circularly polarized light beam are produced after the two returning light beams traverse a quarter wave plate oriented at 45 degrees. The vector sum of these two circularly polarized light beams is identical to a linearly polarized light beam with its inclination angle relative to the horizontal axis that varies with the motion of the object. This resultant, a linearly polarized light beam, is then divided into two light beams by a non-polarization beamsplitter. These two polarized beamsplitters PBS3 and PBS4, whose axes are 45 degrees apart, are utilized to create the 90 degrees phase difference of the light beam intensity signal measured at the photodiodes. Velocity and position signals can be easily decoded using the signal processing schemes. The returning beams E_1 and E_2 can be expressed as

$$E_1 = \begin{bmatrix} 1 \\ 0 \end{bmatrix} e^{i2\pi(f_l + f_{d1})t} \tag{1}$$

$$E_2 = \begin{bmatrix} 0 \\ 1 \end{bmatrix} e^{i2\pi(f_l + f_{d2})t + \phi} \tag{2}$$

where f_l is frequency of the incident laser beam, and f_{d1} and f_{d2} are the Doppler frequencies due to the specimen

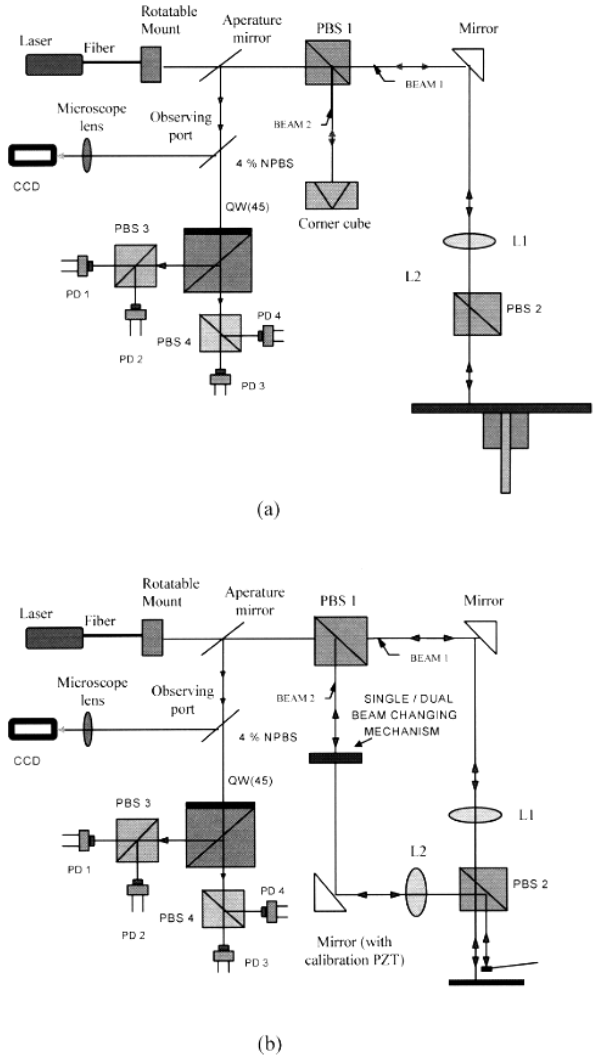

Figure 7. The two internally convertible optical configurations, which are (a) single beam and (b) dual beam, of a laser Doppler vibrometer/interferometer.

motion. This can be shown clearly after the two returning object beams pass through the quarter waveplate. The recombined light vector can be expressed as follows:

$$E = \left\{ \begin{bmatrix} 1 \\ \mathrm{i} \end{bmatrix} \mathrm{e}^{\mathrm{i}2\pi f_{d1} t} + \begin{bmatrix} \mathrm{i} \\ 1 \end{bmatrix} \mathrm{e}^{\mathrm{i}2\pi (f_{d2} t + \phi)} \right\} \times \mathrm{e}^{\mathrm{i}2\pi f_l t} \tag{3}$$

which is the vector sum of the two circularly polarized light waves and can be viewed as a linearly polarized light with its polarization axis located at $[2\pi(f_{d2} - f_{d1})t + \phi]/2$. If the amplitudes of the two light beams are identical, the recombined light vector is a linearly polarized light beam whose plane of polarization rotates through 360 degrees when the optical path difference between the two light beams equals two wavelengths. Since the spatial axes of the two polarization beamsplitters are 45 degrees apart, the quadratural signals detected from the photodiodes can be expressed as

$$I_1 \propto \left[1 + \sin\left(2\pi\left(f_{d2} - f_{d1}\right)t + \phi\right)\right] \tag{4}$$

$$I_2 \propto \left[1 + \cos\left(2\pi\left(f_{d2} - f_{d1}\right)t + \phi\right)\right]. \tag{5}$$

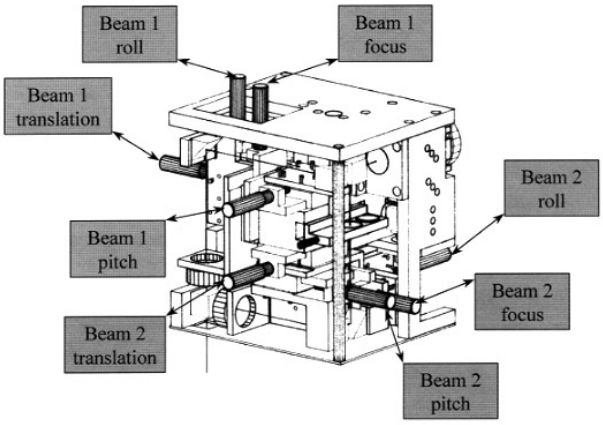

Figure 8. The isometric view of the newly designed interferometer system for miniature piezoelectric actuator performance evaluations.

If we perform a standard quadrature signal detection of the above two signals, the relative position between the two object surfaces can be obtained in real time. Furthermore, if the electric signals from the detectors are mixed with another electronically generated cosine and sine signal with frequency f_c separately, we can obtain the following:

cosine channel :

$$\cos\left[2\pi\left(f_{d1} - f_{d2}\right)t + \phi\right] \cos\left(2\pi f_c t\right) = \tfrac{1}{2}\left\{\cos\left[2\pi\left(f_d + f_c\right)t + \phi\right] + \cos\left[2\pi\left(f_d - f_c\right)t + \phi\right]\right\} \tag{6}$$

sine channel :

$$-\sin\left[2\pi\left(f_{d1} - f_{d2}\right)t + \phi\right] \sin\left(2\pi f_c t\right) = \tfrac{1}{2}\left\{\cos\left[2\pi\left(f_d + f_c\right)t + \phi\right] - \cos\left[2\pi\left(f_d - f_c\right)t + \phi\right]\right\} \tag{7}$$

where $f_d = f_{d2} - f_{d1}$ is the relative Doppler phase shift created by the two specimen surfaces. Summing these two signals yields an output signal of $\cos[2\pi(f_d + f_l)t + \phi]$. Sending this signal into a simple frequency-to-voltage converter yields a velocity signal due to the Doppler effect. Thus this newly developed differential laser Doppler interferometer can measure both velocity and displacement. In addition, to increase the structural rigidity of the interferometer (figure 7) so as to minimize the relative deformation that may appear in the differential paths of the optical system, a new mechanical configuration (figure 8) was designed to arrive at this goal.

To measure miniature parts such as piezoelectric actuators, the measurement locations have been becoming more difficult to identify accurately. As our AVID system is capable of measuring relative displacement or the velocity of two locations of a small test specimen, the difference and the location of the two measurement points are important for angle identification of the specimen under testing. To meet this requirement and to correct the location measurement errors, a microscopic imaging system was designed to provide accurate measurement location positioning and to retrieve the testing surface image when an external light source is added. In other words,

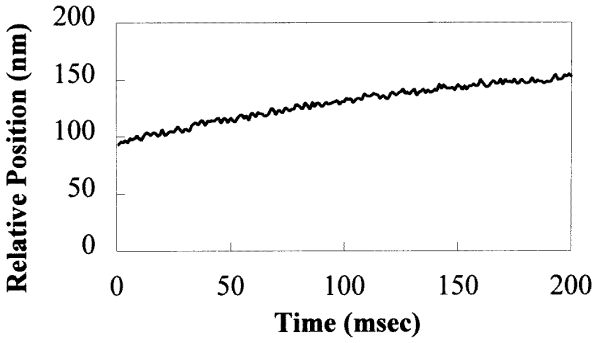

Figure 9. Displacement signal of a magnetic disk drive test sample obtained by AVID.

to make this system even more suitable for miniature piezoelectric actuators evaluation, a built-in microscopic measurement feature was designed into the interferometry system described above to become an AVID, advanced vibrometer/interferometer device (Lee *et al* 1996, AHEAD 1997). The charge coupled device (CCD) imaging system and the imaging lens (figure 7) are placed behind the observing port, which work in conjunction with the two focusing lenses L1 and L2, to form a microscopic system. During alignment, the imaging lens is positioned to measure the angle and location of the two returning light beams. Once the testing surfaces are positioned correctly relative to AVID, the image lens can be positioned to have the measurement surface (or measurement surfaces for the two-beam configuration shown in figure 7(b)) shown clearly on the CCD. A frame grabber was used to transfer the CCD captured image to the personal computer, where the image captured was used to perform further analysis.

To evaluate the performance of AVID, an N58 slide typically used in magnetic disk drives was attached to a small piezoelectric actuator and placed on top of a typical magnetic thin film disk to mimic nanometer flying. A high-speed PC based analog-to-digital converter (Gage 1995) was used to record the quadrature signal generated by AVID as indicated in (4) and (5) to give AVID a bandwidth of 20 MHz, which is almost 50 times wider than the best commercially available interferometer. The two measurement light beams were placed on top of the slider and on top of the disk, respectively. The experimental data obtained are shown in figure 9.

4. Stack type actuators

Mechanically magnifying mechanisms based on the lever principle have long been developed to overcome the problem where piezoelectric material can only generate very small deformations (Sakamann 1980, Takahashi 1985, Ota *et al* 1985, Fukui *et al* 1986, Kitagawa 1986, Sakurai *et al* 1987, Asano 1987). Several ultra-high-resolution piezoelectric stages based on these mechanisms were developed at the NTU MEMS Collective and will be discussed in this section.

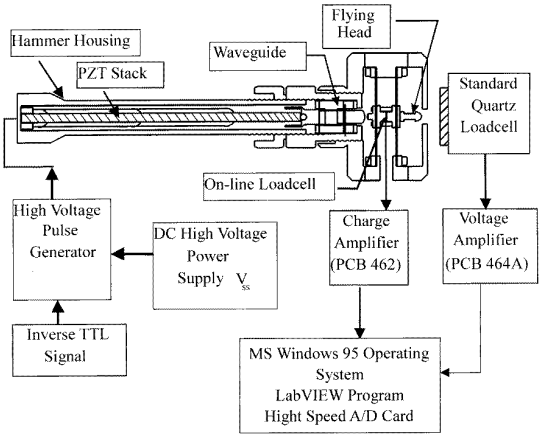

Figure 10. Schematic of the impact hammer system design/calibration.

4.1. Impact hammers

To achieve large motion, Chang and Wang (1988, 1990) first invented a piezoelectric impact hammer, which was designed by using the waveguide concept. Lee and Wu (1993) later improved this particular mechanism. An on-line loadcell (OLC) was added to the free-flying object to detect the impact force. The basic layout of this newly developed ultra-high-precision, high-speed impact hammer system is shown in figure 10. The steel ball located between the PZT top holder/waveguide (H03 of figure 11) and the PZT stack (H13 of figure 11) is used to make sure the force transmitted between the PZT top holder/waveguide and the PZT stack will be straight. The pre-load spring (H06 of figure 11) is being used to control the externally applied pre-load so as to optimize the momentum transfer.

As the capacitance value of the piezoelectric stack shown in figure 11 is in the range of 1.25 μF, a normal power supply will not be able to provide enough current to drive the piezoelectric stack. A large amount of charge was stored within a set of high-value high-voltage capacitors first, and then all the charge was released to drive the piezoelectric stack.

The set-up shown in figure 10 was used for the impact hammer calibration and for performance evaluation. A PCB model 209A (PCB 1994) Standard Quartz Loadcell (SLC) of 8.1 mV g^{-1} sensitivity was used as the calibration sensor. The graphic user interface software LabVIEW (National Instruments 1993) was used to communicate with a Gage card (Gage 1995) of 250 MHz sampling rate to record the signal generated from the OLC and the SLC. The sensitivity of the OLC can be obtained by comparing the signal between the OLC and the SLC.

The experimental data (figure 12) obtained by the OLC indicate that several impulses are present for each impact. The first impulse represents the impact forces transmitted by the PZT stack to the flying head. The second impulse represents the interaction between the flying head and the test specimen. The data clearly indicate that the impact time generated is in the range of microseconds. The impact location repeatability and timing accuracy of the impact hammer system was also examined. A total of ten sets of

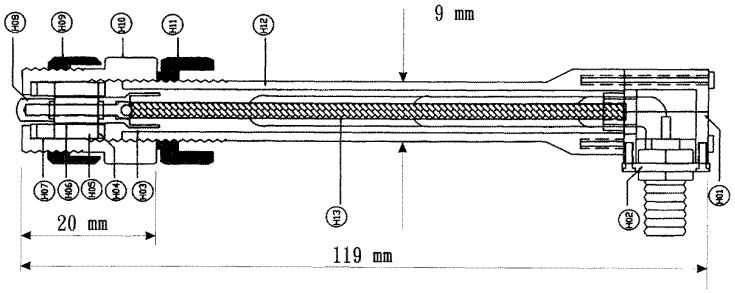

H01:connecter
H02:cover plate
H03:PZT top holder/waveguide
H04:screw holder
H05:spring spacer
H06:pre-load spring
H07:screw holder
H08:waveguide top header (screw in)
H09:lock 1
H10:pre-load top housing
H11:lock 2
H12:PZT rod housing
H13:PZT stack

Figure 11. Schematic of the impact hammer driver.

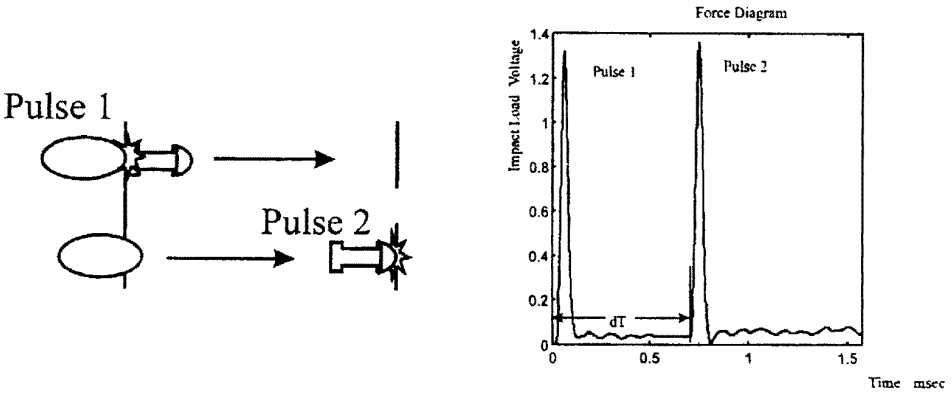

Figure 12. The impulses sensed by OLC.

pulses generated by the OLC were recorded by using a Gage card. All of these signals were triggered by an inverse TTL signal used to initiate the piezoelectric driving mechanism. The variations of the flying time dT between the first two pulses was measured to be far less than 1 μs. The impact location accuracy was examined by checking the center impact mark location difference for a single impact and for a set of ten consecutive impacts under the same condition and at the same location. The impact location accuracy was found to be in the range of 1 μm. These sets of data clearly verify the performance achievable by piezoelectrically driven impact systems.

4.2. Dual dimensional scanner

High-speed scanners play important roles in many recent industrial applications including laser printers, optical storage devices and inspection instruments. The common requirement of these types of scanner is that they have fast dynamic response, high resolution and miniature dimensions.

Steinhaus and Lipson (1979) described a flexible mirror constructed from a laminated glass plate and piezoelectric ceramic. The geometry of the mirror could be changed by the deformation of the laminated structure when an electric voltage is applied. Okuda *et al* (1986) developed a laser scanner using a stacked piezoelectric actuator to achieve a 0.01 mrad V^{-1} scanning range and a 1.6 kHz resonant frequency at both X and Y axes. More recently, Cunningham *et al* (1995) described a reflecting mirror attached to the end of a small cantilever to detect vibration using a quadrant detector operating at the resonant frequency of 1.4 kHz.

The scanner design presented in figure 13 is a new mechanism which adopts a multi-layered piezoelectric actuator to achieve high-frequency optical scanning in dual dimensions. The basic construction of the scanner includes a piezoelectric actuator, two V-shaped reflecting surfaces mounted on a triangle mass, two supporting beams and a driving plate connecting the two driving beams. When the scanner is operated at the resonant frequency, the reflecting surfaces oscillate at the corresponding vibration modes. The incident light will then be reflected accordingly to perform the scan function. In the design shown in figure 13, the dual-dimension scan is achieved by oscillating the scanner at two distinct resonant modes. Driving the piezoelectric actuators electrically induces the resonant motion. The symmetric design enlarges the total reflecting

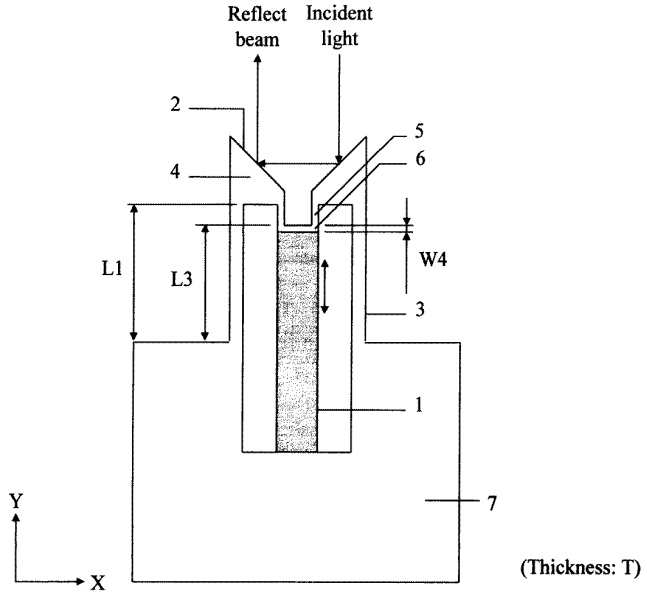

Figure 13. Schematic design of a scanning mechanism, with 1: piezoelectric actuator, 2: reflecting surface, 3: supporting beam, 4: triangle mass, 5: driving beam, 6: driving plate and 7: base plate.

angle. More specifically, whenever the reflecting surface rotates at angle θ, the incident light beam will be reflected by 2θ angles at each V shaped reflecting surface which results in a total of 4θ reflecting angles. With the tight closed loop mechanical design adopted, the scanner can be operated at a high resonant frequency. Furthermore, this design also reduces geometric error induced by thermal drift.

The multi-layered piezoelectric ceramic stack measures 2 mm $\times$ 3 mm $\times$ 10 mm and serves as the actuator to provide force and displacement to the mechanism. It offers a maximum displacement of 9.1 μm at 150 V DC, generates 200 N force and is resonant at 138 kHz. When subjected to an externally applied voltage, the d_{33} mode piezoelectric actuator oscillates longitudinally in the Y-direction as shown by the double arrow in figure 13. Using the actuator as the excitation source, the driving plate attached to the actuator in turn excites the driving beams, the triangle masses and the supporting beams.

Fabricating the scanner involves two steps: machining the base plates and the elastic beams from a metal blank, and installing the piezoelectric actuator into the machined metal blank. The scanner itself was machined from a 3 mm thick 6061-T6 aluminum blank. The overall dimension of the scanner is 5 mm $\times$ 8.5 mm $\times$ 3 mm. Preventing the degenerate vibration modes of this complex structure, the geometry and dimension of the mechanism were precisely maintained. Special attention was paid to mechanical components such as the supporting beam and the driving beam, which are shown to have strong influence on the resonance of the scanner by finite-element analysis. To meet the stringent requirements of these parts, a precision wire-cutting process was used to fabricate the scanner. The installation of the piezoelectric actuator was also found to be very important. The adhesion between the piezoelectric actuator and the mechanism must be in complete surface contact. The flatness and parallelism of the surface which adapts the actuator should be precisely maintained. The actuator should also be placed in a precise location to avoid having lateral forces exerted on the mechanism.

Mode shapes were used to control the dual-dimension motion of the scanner. The vibration modes used including the first and second bending, and the first and second torsion. Figure 14 illustrates the respective vibration modes and the corresponding scanning path of the reflected light beam. Only the bending modes used in the optical scan of the X- and Z-direction are to be discussed in detail herein as the scanning path induced by other resonant modes can be easily inferred from the discussion of the bending modes. It is clear from figure 14 that the torsion modes are also good for scanning in the X–Z-plane. One of the critical design goals was to separate the resonant frequencies far from each other to avoid the coupling effect among these modes.

Similar to the requirement for scanners, the primary requirement of our scanner was to possess both high resonant frequency and a wide scanning range. In addition, to achieve a modal de-coupling requirement of the scanner, the dominant parameters of the mechanism as shown in figure 13 were extensively studied to observe their influence. In this study, the ANSYS (Swanson 1993) finite-element method (FEM) software was used to perform the required modal analysis. Three-dimensional structure elements were used to construct the finite-element model in order to observe the mode shape clearly. The electro-mechanical coupling element in ANSYS was used to simulate the electrical and mechanical behavior of the piezoelectric actuator used.

Using ANSYS, the resonant frequency and the corresponding mode shapes of the mechanism were computed and identified in detail. The final dimension chosen was determined from a parametric analysis. The

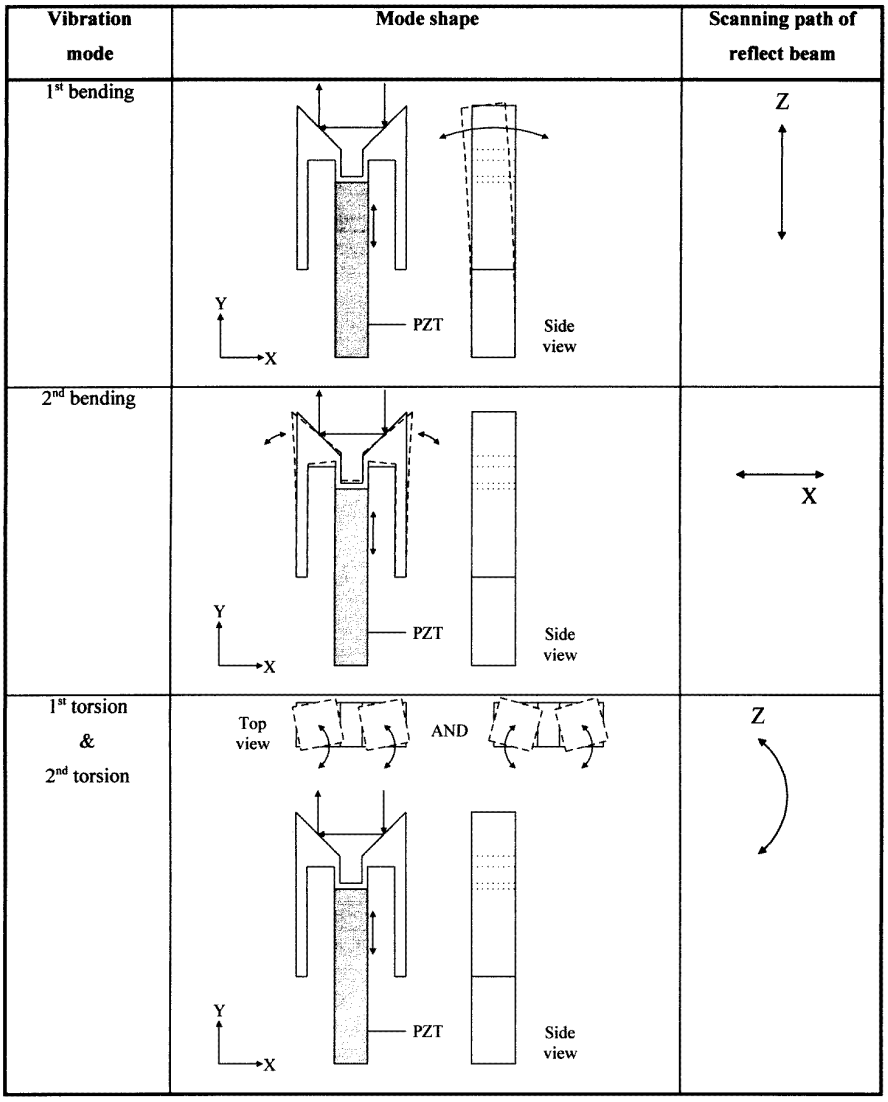

Figure 14. Vibration modes of the scanning mechanism used to reflect the light beam.

calculated resonant frequencies of the first two bending modes were 19 707 Hz and 50 977 Hz respectively, and of those the first two torsion modes were 37 018 Hz and 44 601 Hz, respectively.

To verify the scanner performance, the scanner designed by using ANSYS was fabricated and its performance was experimentally evaluated by mechanical, electrical and optical measurements. Our mechanical measurement investigated displacement sensitivity, resonant frequencies and the vibration modes of the scanner. The displacement sensitivity was measured by using a laser interferometer mentioned above (Lee *et al* 1996, AHEAD 1997) that has a measuring resolution of better than 2 nm and a bandwidth of 20 MHz. The laser interferometer measures the scanner motion at different positions to investigate the resonant frequencies and the corresponding vibration modes. The DSA function of AVID (AHEAD 1977), which is similar to the dynamic signal analyser (Hewlett Packard 1991) was used to perform a transfer function measurement and the piezoelectric actuator driven by an output source signal of the DSA was used as the excitation source. The displacement data measured by the laser interferometer were used as the output response signal to be fed into the dynamic signal analyser. From the measured frequency response functions, the resonant frequencies were then found and the corresponding vibration modes were also identified by the typical modal testing procedure. The measured resonant frequencies for the first and second bending modes occurred at 23.8 and 48.8 kHz respectively, and at 34.2 kHz and 44.7 kHz for the two torsion modes respectively. These results agree well with the FEM analysis results except for the first bending mode.

Our electrical measurements, which adopted a Tektronix current probe (Tektronix 1987) to measure the electric current through the piezoelectric actuator during the swept excitation, was used to further investigate the resonant and anti-resonant frequency of the electrical system of the newly developed scanner. The resonant frequency for the bending modes was found at 23.98 kHz and 48.5 kHz respectively, and 36.13 kHz and 44.38 kHz respectively for

the two torsion modes. The anti-resonant frequency of the first bending mode was also found at 25.74 kHz where the local minimum current existed. From the resonant and anti-resonant frequencies for the first bending mode, the electro-mechanical coupling coefficient was found to be 0.364.

Finally, the scanning performance of the scanner was measured by performing an optical measurement. The positions of the reflected laser beam projected to a plane parallel to the X–Z-plane were dynamically measured by a 0.1 μm resolution quadrant detector. The light source used is a 15 mW He–Ne laser. The calibration of the quadrant detector was conducted first to correlate to the given displacement of the light beam with its output electrical voltage. The scanner was operated to its first two bending modes and the scanning range was detected by using the quadrant detector. The reflection angle sensitivity of the scanner was calculated from the quadrant detector output data. The measured reflection angle sensitivities were 88.76 and 19.29 μrad V^{-1} when operating at the first and the second bending modes respectively. The maximum reflection angles for the scanner were found to be 13.3 mrad and 2.89 mrad respectively.

4.3. Langevin type ultrasonic motors

Ultrasonic motors, featuring a simple structure, high torque and low speed, have been actively studied. These motors use contact forces to cause the rotors to rotate. For a traveling-wave ultrasonic motor, a bending wave traveling in a ring or a disk generates the contact force on the rotor. This type of ultrasonic motor has been applied to auto-focusing lenses (Hosoe 1989). For a Langevin ultrasonic motor, a combined longitudinal and torsional vibration in a cylindrical rod produces intermittent contact forces to drive the rotor (Ohnishi *et al* 1993). Compared with a traveling ultrasonic motor of the same diameter, its torque is larger by one order of magnitude. This type of ultrasonic motor developed at the NTU MEMS Collective will be discussed in detail in this section.

A typical multi-mode vibrator type ultrasonic motor (figure 15) can be separated into three parts. The first part is a cylindrical stator used to produce the normal and the tangential motions at its end surfaces. The second part includes two separate vibrators to generate longitudinal and shear vibrations in the stator. The third part adopts a rotor to convert the vibratory motion at the stator surface into a rotary motion. In a typical stator configuration, longitudinal waves propagate at a much higher speed than shear waves. The resonant frequencies of these two modes are thus different without special design considerations. However, if the rotor is to be operated smoothly, the longitudinal and the shear modes must be of the same frequency and must be synchronized. To achieve our Langevin ultrasonic motor design goal, a 'neck' as shown in figure 15 was made in the stator to shorten the propagation length of the shear wave while keeping that of the longitudinal wave nearly unchanged.

An experimental ultrasonic motor design based on the above-mentioned concept was constructed in the laboratory. The motor (made of brass) was designed to operate

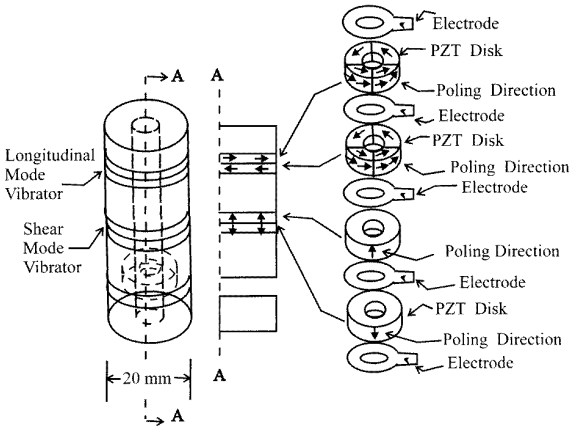

Figure 15. Exploded view of the ultrasonic motor.

at a driving frequency of 40 kHz. The longitudinal wave and shear wave velocities in brass are 3672 and 2298 m s^{-1}, respectively. As the stator should have a total length approximately equal to one half wavelength of the longitudinal mode, it was designed to be around 46 mm. Using ANSYS to analyse the resonant frequencies of the stator, the length was determined to be 41 mm with a neck located 10 mm from the end surface (figure 15). The resultant design, which is 20 mm in diameter, had a first longitudinal mode at 39 588 Hz and a first shear mode at 39 734 Hz.

Two sets of PZT disks were used to drive the motor (figure 15). The PZT disks (Keramos, K-270) had the electromechanical coupling coefficients $k_{33} = 0.7$ and $k_{15} = 0.71$ (Keramos 1993, Valpey-Fisher 1995). Two shear mode disks, each consisting of four PZT plates, were located 13 mm from the stator–rotor interface to generate tangential motion at the interface. Two longitudinal mode disks located 22 mm from the interface were used to generate the normal motion. Driving these two sets of disks from the same power supply with an appropriate phase difference induced rotor motion (figure 15).

Experimental data indicate that this motor had a peak speed of 30 rpm at a zero external load when it was driven by a 72 V_{RMS} power supply. This rotation speed dropped to 15 rpm at a load of 4×10^{-3} N m. The efficiency at this speed was computed to be around 20%. These data indicate that a simple Langevin type of ultrasonic motor has been successfully designed and demonstrated.

4.4. Linear micro-positioner with long travel range

The goal of the micro-positioning stage was to provide a precision linear positioning mechanism with a long travel range. The schematic representation of the micro-positioning stage to be discussed is shown in figure 16. The arrows in the figure indicate the stage component motion. The stage consists of an amplifying device and a parallel leaf spring guiding device. The amplifying device used to amplify the length changes of the piezoelectric actuator, component 1, is composed of a multiple Scott–Russell mechanism (Martin 1982) that is indicated by components

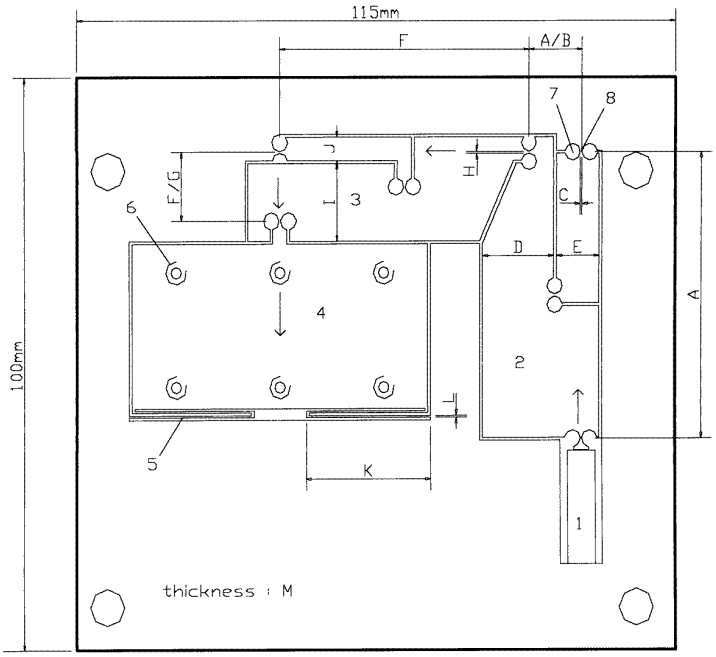

Figure 16. Schematic representation of the micro-positioning stage. 1: PZT, 2: the first linkage, 3: the second linkage, 4: platform, 5: leaf springs, 6: tapped hole, 7: cut-out slot to form flexure hinges, 8: flexure hinges. The key dimensions are represented by the control factors *A* to *M*.

2 and 3 in figure 16. The parallel leaf spring guiding device guided the stage platform motion and prevented lateral displacement and angular deviation. The flexure hinges fabricated with a single metal blank can avoid backlash, stick–slip friction and the need for lubricants. Components 1 to 5 were connected in sequence to transmit the motion of the actuator to the platform.

The motion of the components in the micro-positioning stage is described as follows. The length of the piezoelectric actuator, component 1, changes with the externally applied driving voltage on the piezoelectric actuator. This length change pushes or pulls the input terminal of the first stage of the Scott–Russell linkage, component 2, and causes displacements at the output terminal of the linkage. Similarly, the second stage of the Scott–Russell linkage, component 3, is driven by the output displacement of component 2. Finally, the platform, component 4, moves due to the output motion of the second linkage. The leaf springs, component 5, joined to the platform can offer a reaction force to prevent the platform from rotating and moving laterally. The two stages of the Scott–Russell linkage were designed to amplify their input displacements so that the derived travel range of the platform is significantly larger than the range of the length changes of the actuator.

The overall design problem for this stage lay in how to optimize the geometry and the configuration of the flexure hinges and the Scott–Russell linkages. The goal was to achieve a maximum mechanical displacement gain and a minimum lateral displacement while taking into account the demands imposed by the stretch and bending of the flexure hinges and linkages. As the Taguchi method for quality engineering (Ross 1988) is a method for searching for performance, quality and cost optimization, it was adopted to solve our type of design problem. Its essence is to identify the optimal values of the control factors such as stage design variables by using orthogonal arrays, signal-to-noise (S–N) ratios and analysis of variance (ANOVA). A total of thirteen control factors respectively denoted by A, B, C to M were used in this design optimization case. The physical meaning of each control factor is shown in figure 16. The thirteen factors can be assigned to an L_{27} orthogonal array that is the most possible economical array. After completing all trials and finishing with the analysis of the data, the recommended optimum settings of the control factors were found and listed in table 1.

To verify the optimized design, the critical performance of the stage fabricated was measured experimentally using the laser interferometer mentioned above. The measured maximum output displacement was 112 μm at a 100 V driving voltage. The angular deviation of the output platform was also evaluated. The angular motion of the stage was found experimentally to be less than 0.278 μrad for a 1 μm output displacement at a low excitation frequency. This performance translates to a maximum angular deviation of 31.136 μrad at a 112 μm maximum output displacement.

Smooth linear output displacements as a function of the applied voltage were expected. Figure 17 shows the measured displacements as a function of the voltage applied to the piezoelectric driving element. In figure 17, the signal designated as voltage 1 is the sinusoidal wave from a function generator option of AVID measured by using a 10$\times$ probe, i.e., a 1 volt recorded signal represents a 10 volts driving voltage. The AVID displacement signal was used to measure the platform motion, and shown as the

Table 1. Optimum level for each control factor. All factors are in mm, except that *B* and *G* are dimensionless.

			Optimum result	
			Level	Value
1st linkage	total length	*A*	1	50
	amplifying factor	*B*	3	5.0
	width of flexure hinge	*C*	2	0.4
	parameter for width of link 1	*D*	3	13.5
	parameter for width of link 2	*E*	1	8.5
2nd linkage	total length	*F*	3	48.0
	amplifying factor	*G*	1	4.0
	width of flexure hinge	*H*	1	0.3
	parameter for width of link 1	*I*	3	13.5
	parameter for width of link 2	*J*	1	4.0
Leaf spring	parameter for length	*K*	3	24
	width	*L*	1	0.3
Thickness of whole stage		*M*	3	10.0

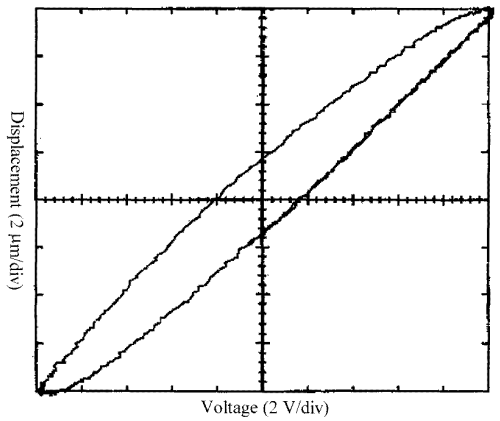

Figure 17. The measured hysteresis curve without compensator.

displacement in figure 17. The experimental data shown in figure 17 clearly demonstrate that hysteresis in the stage induces about 22.5% of the maximum displacement offset upon return to 0 V.

To reduce the hysteresis of the piezoelectric-actuated stage, a simple open-loop technique (Duong and Garcia 1995) was used. This open-loop compensator is able to compensate for the phase lag inherent in the piezoelectric stage. It used a phase-lead compensation analog circuit that required no feedback from the output member of the stage so as to make the whole controlled system simple. The phase-lead compensation circuit was placed between the power amplifier and the piezoelectric actuator while the function generator signal was treated as the command signal. The transfer function of the circuit was chosen so that it canceled out the frequency dependent phase lag of the stage over the low excitation frequency range. The excellent performance of the compensated hysteresis of the piezoelectric stage shown in figure 18 is a testimony of the effectiveness of this phase-lead compensation scheme.

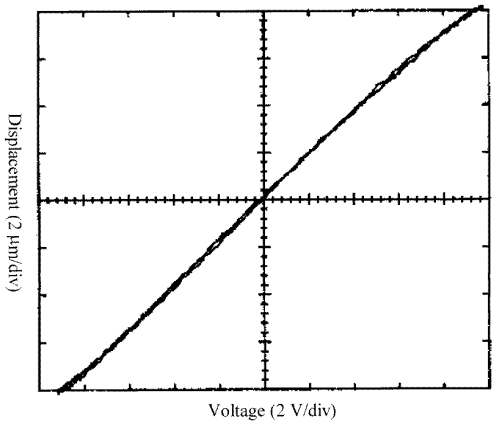

Figure 18. The measured hysteresis curve with a compensator.

A wide dynamic operating range is needed for a precision-positioning device. The dynamic signal analyser (Hewlett Packard 1991) was used to measure the frequency response between the stage displacement and the input voltage. The first natural frequency of the system was found to be 83.5 Hz. The step response of the output member of the stage revealed that the settling time of the stage is approximately 50 ms at 10% full travel range. To identify the finest resolution of the stage, a stairway-type command signal was used to drive the piezoelectric actuator of the stage. During the experiments, the applied voltage of each 'stairway' was attenuated successively to determine the lowest input that the stage response could still distinguish. The stage displacement resolution was determined to be 0.04 μm. The experimental data obtained testify to the validity of the design methodology described in this section for designing long-travel-range piezoelectric micro-positioning stages.

5. Conclusions

Piezoelectric materials have long been known for their capability to output large forces and pack very high energy density into a small volume. These excellent properties have made piezoelectric materials one of the primary candidates to drive miniature mechanisms. However, the difficulties of fabricating a miniature piezoelectric actuator and the small displacement that piezoelectric actuators can exert imposes some shadow on piezoelectric actuators being further adopted. To further promote the rapid development of miniature piezoelectric actuators, the sputtering processes for ZnO and PZT, that are important for miniature laminated piezoelectric actuators, have been examined to identify the important parameters for making sputtered piezoelectric materials of high polarization profiles.

A newly developed laser Doppler interferometer that was especially designed for evaluating the performance of miniature piezoelectric actuators was also described. This laser Doppler interferometer adopted a circular polarization interferometer configuration so as to arrive at a miniature yet rigid structure for high-precision measurements. The

built-in microscope provides the user with an *in situ* observing capability. In addition, the microscope serves as an excellent tool for locating measurement location accurately. Combining these characteristics with the better than 2 nm displacement measurement resolution and the DC to 20 MHz bandwidth, makes this laser Doppler interferometer an excellent tool for evaluating miniature piezoelectric actuator performance.

The use of piezoelectric lamina in a laminated structure consisting of a beam, plate and shell, is now being viewed as a mechanical transformer that can convert the large-force small-displacement characteristics of a piezoelectric actuator into a small-force large-displacement configuration. The importance of this design concept in the development of laminated piezoelectric actuators was reviewed. The importance of effective pressure resultants was mentioned to further point out the potential trap in designing curved type piezoelectric actuators.

Other magnifying mechanisms, which include waveguides, resonance and mechanical levers, that can also convert large-force small-displacement piezoelectric material characteristics into a smaller-force large-displacement actuator are examined in detail as well. A high-precision piezoelectric impact hammer, which can be used as an impact testing tool and was designed based on the waveguide concept, was developed and tested. The large-force, large-displacement behavior exerted by the piezoelectric hammer testifies to the validity and efficiency of adopting the waveguide concept in designing piezoelectric actuators.

A dual-dimensional scanning piezoelectric mirror operated by exciting the structures in different resonant modes was designed, constructed and evaluated. The performance parameters obtained for this type of piezoelectric actuator attest to the effect of this design concept. A Langevin type ultrasonic motor that transformed the resonant vibrating modes into a circular motion and arrives at a very large traveling range was designed, improved and fabricated. The successful test-run of this motor further certifies to the importance of miniature piezoelectric actuators.

For ultra-high-precision positioning requirements, a piezoelectric positioning stage designed based on the mechanical lever principle was designed and optimized. The phase-lead open loop compensator approach was adopted to reduce the hysteresis effect of the piezoelectric actuators. The 0.04 μm resolution achieved by this stage reassures us of the potency of the mechanical level design and the phase-lead compensator.

With the design concept elaborated, the evaluation tools developed, the mechanical magnifying mechanism refined and the hysteresis reduction approach detailed, all have revealed the many frontiers that have yielded to research and development efforts in the search to further advance miniature piezoelectric actuator technology.

Acknowledgments

The authors gratefully acknowledge the support of the National Science Council of Taiwan, Republic of China, under project numbers NSC 84-2623-D-002-002, NSC 85-2221-E-002-051, NSC 85-2221-E-002-052, NSC 85-2221-E-002-053, NSC 85-2612-E-002-056, NSC 86-2212-E-002-040, NSC 86-2212-E-002-094, NSC 86-2212-E-002-096 and CS 86-0210-D-082-004.

References

AHEAD Optoelectronics 1997 AVID, advanced vibrometer/interferometer device B1, No 130, Sec. 3, Keelung Road, Taipei, Taiwan, Republic of China. Tel: (+886) 2 369-1520, Fax: (+886) 2 362-0485

Asano H 1987 Stacked piezoelectric ceramics displacement magnifying devices *US Patent* 4 703 215

Bailey T and Hubbard J E 1985 Distributed piezoelectric-polymer active vibration control of a cantilever beam *J. Guid. Control* **8** 605–11

Baltes H 1993 CMOS as sensor technology *Sensors Actuators* A **37–38** 51–6

Chang P S H and Wang H C 1988 Matrix printer actuator *US Patent* 5 046 872

——1990 A high speed impact actuator using multilayer piezoelectric ceramics *Sensors Actuators* **24** 239–44

Chou J M 1997 Laminated piezoelectric shells: design, processing and experiments *PhD Dissertation* Institute of Applied Mechanics, National Taiwan University

Cunningham M J, Jenkins D F L, Clegg W W and Bakush M M 1995 Active vibration control and actuation of a small cantilever for applications in scanning probe instruments *Sensors Actuators* A **50** 147–50

Duong K and Garcia E 1995 Open loop compensation in a stack-mass positioning system *J. Intell. Mater. Syst. Struct.* **6** 292–6

Fukui I, Hamatsuki T, Yano T, Sato E and Inui O 1986 Impact printer head capable of printing a dot at a distance narrower than a thickness of a printer unit *US Patent* 4 589 786

Gage 1995 *Technical Reference and User's Guide for CompuScope 250* (Montreal: Gage) pp 4.1–4.15

Hewlett Packard 1991 *35665A Dynamic Signal Analyzer Operation Manual* (Everett, WA: Hewlett Packard)

Hosoe K 1989 Ultrasonic motors for auto-focusing lenses *Ultrason. Technol.* **1** 36–41

Keramos 1993 *The General Characteristics of Crystal Quartz Materials* (Indianapolis, IN: Keramos)

Kitagawa K 1986 Printing mechanism for dot matrix printers *US Patent* 4 613 241

Lee C K 1987 Piezoelectric laminates for torsional and bending modal control: theory and experiment *PhD Dissertation* Cornell University

——1990 Theory of laminated piezoelectric plates for the design of distributed sensors/actuators. Part I: governing equations and reciprocal relationships *J. Acoust. Soc. Am.* **87** 1144–58

Lee C K and Moon F C 1989a Laminated piezopolymer plates for torsion and bending sensors and actuators *J. Acoust. Soc. Am.* **85** 2432–9

——1989b Laminated piezopolymer plates for torsional and bending modal control *US Patent* 4 868 447

Lee C K, Wu G Y, Pan, G T, Chiang S R and Wu J 1996 An innovative miniature differential laser Doppler interferometer *Int. Symp. on Polari. Ana. and Appl. to Devices Tech (Yokohama, 1996)*

Lee C K and Wu T W 1992 New differential laser interferometer/vibrometer for nanometer structural displacement/vibration measurements *IBM Tech. Disclosure Bull.* **35** 189–95

——1993 Piezoelectric hammer with on-line loadcell *IBM Tech. Disclosure Bull.* **36** 175–8

——1995 Differential laser interferometer for nanometer displacement measurements *AIAA J.* **33** 1675–80

MacDonald G A 1990 A review of low cost accelerometers for vehicle dynamics *Sensors Actuators* A **21** 303–7
Martin G H 1982 *Kinematics and Dynamics of Machines* (New York: McGraw-Hill)
Marty J, Malki A, Renouf C, Lecoy P and Bailleu F 1995 Fiber-optical accelerometer using silicon micro-machining techniques *Sensors Actuators* A **47** 470–3
Mason W P 1950 *Piezoelectric Crystals and Their Application to Ultrasonic* (New York: Van Nostrand)
Mechanical Engineering 1992 *MEMS—Microelectromechanical System* (American Society of Mechanical Engineers) pp 40–7
Motamedi M E and White R M 1994 Acoustic sensors *Semiconductor Sensors* ed S M Sze (New York: Wiley)
National Instruments 1993 *LabVIEW for Windows* (Austin, TX: National Instruments)
Ohara Y *et al* 1993 PZT–polymer piezoelectric composites: a design for an acceleration sensor *Sensors Actuators* A **36** 121–6
Ohnishi O, Myohga O, Uchikawa T, Tamegai M, Inoue T and Takahashi S 1993 Piezoelectric ultrasonic motor using longitudinal–torsional composite resonance vibration *IEEE Trans. Ultrason. Ferroelectr. Frequency Control* **UFFC-40** 687–93
Okuda M, Wakita N, Ohya K, Banno H and Hattori S 1986 A laser scanner using stacked piezoelectric ceramic actuator *Japan. J. Appl. Phys.* **25** (Supplement 1) 223–5
Ota T, Uchikawa T and Mizutani T 1985 Printing flight hammer using multi-layer piezoelectric actuator *Japan. J. Appl. Phys.* **24** (Supplement 2) 41–5
PCB 1994 *Transducer Instrumentation: Model 209A Force Transducer* (Depew, NY: PCB Piezotronics)
Radiant Technologies 1992 *Operating Manual, RT66A Standardized Ferroelectric Test System* (Albuquerque, NM: Radiant)
Rogacheva N N 1980 Equations of electro-elasticity for free piezoceramic shells *Mech. Solids* **15** 122–30
——1994 *The Theory of Piezoelectric Shells and Plates* (Ann Arbor, MI: Chemical Rubber Company)
Ross P J 1988 *Taguchi Techniques for Quality Engineering* (New York: McGraw-Hill)
Sakamann W 1980 Matrix printer with piezoelectrically driven printing needles *US Patent* 4 193 703
Sakurai K, Suga M and Inoue T 1987 Investigations on an ultrasonic piezoelectric printer *Japan. J. Appl. Phys.* **26** (Supplement 1) 141–3
Sonti V R and Jones J D 1996a Dynamic effects of piezoactuators on the cylindrical shell response *AIAA J.* **34** 795–81
——1996b Curved piezoactuators model for active vibration control of cylindrical shells *AIAA J.* **34** 1034–40
Steinhaus E and Lipson G 1979 Bimorph piezoelectric flexible mirror *J. Opt. Soc. Am.* **69** 478–81
Storgarrd-Larsen T, Bouwstra S and Leistik D 1995 Opto-mechanical accelerometer based on strain sensing by a Bragg grating in a planar waveguide *Proc. Transducers '95* vol 2, pp 667–70
Swanson 1993 *ANSYS Verification Manual* revision 5.0
Tai Y C, Fan L S and Muller R S 1988 IC-processed micromotors: design, technology, and testing *Proc. IEEE Micro Electro Mechanical Systems (Salt Lake City, UT, 1988)* pp 1–6
Takahashi S 1985 Multilayer piezoelectric ceramics actuators and their applications *Japan. J. Appl. Phys.* **24** (Supplement 2) pp 41–5
Tektronix 1987 *AM503 Current Probe Amplifier Instruction Manual* (Beaverton, OR: Tektronix)
Tzou H S 1992 A new distributed sensor and actuator theory for 'intelligent' shells *J. Sound Vib.* **153** 335–49
Tzou H S and Anderson G L 1992 Active piezoelectric shell continua *Intelligent Structural Systems* ed H S Tzou and G L Anderson (Deventer: Kluwer) pp 9–74
Tzou H S and Gadre M 1989 Theoretical analysis of a multi-layer thin shell couple with piezoelectric shell actuators for distributed vibration controls *J. Sound Vib.* **132** 433–50
Tzou H S and Zhong J P 1994 A theory of piezoelectric shell vibration *J. Sound Vib.* **175** 77–88
Valpey-Fisher 1995 *The General Characteristics of Ceramic Materials* (Hopkinton, MA: Valpey-Fisher)
Wu T W and Lee C K 1994a Micro-impact technique and its applications *J. Mater. Res.* **9** 787–804
——1994b Micro-wear technique and its application to ultra thin film systems *J. Mater. Res.* **9** 805–11